machines

MDPI

Article

Fast Simulation and Optimization Design of a Slotless Micro-Motor for High-Speed and High-Flow Pumps

Zhaohai Jin [1,*], Weizhong Fang [1], Jiawei Xu [1], Tianxiong Lu [1], Shitao Yang [1], Li Zhou [1] and Sa Zhu [2]

[1] Hangzhou Easitech Corporation, Hangzhou 310008, China; fangwz@easi-tech.com (W.F.); xujw@easi-tech.com (J.X.); lutx@easi-tech.com (T.L.); yangshitao@easi-tech.com (S.Y.); zhouli@easi-tech.com (L.Z.)
[2] School of Electrical and Power Engineering, Hohai University, Nanjing 211100, China; zhusa@hhu.edu.cn
* Correspondence: jinzh@easi-tech.com

Abstract

The effective part of the winding in a slotless motor varies across different axial sections of the motor, resulting in a three-dimensional structure. Therefore, it is not feasible to simply use the single-section simulation method of conventional radial field motors for motor simulation. Currently, the simulation of slotless motors primarily depends on three-dimensional electromagnetic fields, which present significant modeling challenges and require extensive simulation times, rendering them unsuitable for engineering applications. This paper introduces a method for analyzing slotless motors using a two-dimensional electromagnetic field, based on the electromagnetic field simulation software EasiMotor (R2025). The study elucidates the principle of employing a two-dimensional electromagnetic field to analyze slotless motors and applies this method to the design of a slotless motor with a diameter of 4.5 mm. Through the fabrication of prototypes and performance testing, experimental results validate the accuracy and efficiency of this method.

Keywords: slotless motor; fast simulation; micromotor; EasiMotor

check for updates

Academic Editor: Ahmed Abu-Siada

Received: 6 June 2025
Revised: 18 July 2025
Accepted: 23 July 2025
Published: 24 July 2025

Citation: Jin, Z.; Fang, W.; Xu, J.; Lu, T.; Yang, S.; Zhou, L.; Zhu, S. Fast Simulation and Optimization Design of a Slotless Micro-Motor for High-Speed and High-Flow Pumps. *Machines* **2025**, *13*, 649. https://doi.org/10.3390/machines13080649

Copyright: © 2025 by the authors. Licensee MDPI, Basel, Switzerland. This article is an open access article distributed under the terms and conditions of the Creative Commons Attribution (CC BY) license (https://creativecommons.org/licenses/by/4.0/).

1. Introduction

Slotless motors are widely used in precision control, medical equipment, aerospace, and other fields. In recent years, driven by the development of miniaturized and high-performance drive systems, these motors have shown great promise in emerging applications such as Micro-Electro-Mechanical Systems (MEMSs), drones, and smart wearable devices [1]. Structurally, the slotless permanent magnet synchronous motor comprises permanent magnets, a rotor shaft, a wire cup, and a stator toroidal core. Its defining feature is the absence of teeth and slots in the stator, which confers advantages including low rotational inertia, high efficiency, fast response, and low noise.

A ventricular assist device has gradually evolved from early pulsatile flow pumps to continuous flow pumps. Due to their smaller size and higher efficiency, continuous flow pumps have become the mainstream design and are currently evolving toward high-speed, high-flow miniaturized and intelligent systems [2]. Over the past few decades, rotary blood pumps (RBPs) have achieved significant breakthroughs in the treatment of end-stage heart failure, serving as either a bridge-to-recovery or bridge-to-transplant solution. The compact size, enhanced durability, and improved patient survival rates are driving widespread clinical adoption. Permanent magnet (PM) motors, with their high power density and compactness, are extensively used to drive RBPs [3]. Sahnoune investigated a permanent

magnet synchronous motor (PMSM) for a circulatory assist centrifugal pump in artificial lungs, adopting a hybrid 2D + 3D simulation approach that substituted full-period integration with a four-point sampling method to reduce computational time [4]. Arslan designed a 26,500-r/min, 2 kW high-speed PMSM using a methodology that combined 2D electromagnetic optimization with 3D electromagnetic validation [5]. This dual approach leverages the strengths of each method: 2D simulations offer superior efficiency for parameterized and optimized designs due to reduced computational time, while 3D simulations, despite being more time-intensive, provide critical accuracy for final validation.

Liu investigated control strategies for a 6 mm diameter, 20,000-r/min micro slotless PMSM, achieving satisfactory transient, load, and tracking responses, thereby enhancing the low-speed performance [6]. Yan utilized finite element analysis (FEA) to reduce core losses in a 40,000-r/min high-speed slotless permanent magnet brushless direct current (PMBLDC) motor [7]. Abdi proposed a simplified design methodology for a 60,000-r/min high-speed slotless external-rotor Halbach-array permanent magnet machine, achieving compactness and speed but omitting detailed winding and precision calculations [8].

Lee demonstrated that converting a slotted core motor to a slotless design in a turbomolecular pump increased efficiency by 5.3% (to 97.4%), reduced torque fluctuation from 18.8% to 1.0%, and suppressed vibration and noise [9]. Lower flux density leads to lower iron losses, and a larger effective air gap mitigates flux density variations from magneto-motive force (MMF) harmonics and pulse width modulation (PWM) current ripple, thereby minimizing rotor losses [10]. The slotless motor is ideal for high-speed micromotors. Burnand successfully designed and built a 40,000 r/min motor, with outer dimensions measuring 12.7 mm in diameter and 28 mm in length [11–14].

While slotless motors are characterized by high efficiency and small size, numerous strategies have been proposed to enhance their performance, with studies indicating two in particular:

- New Types of Winding: Burnand et al. designed a novel winding using additive manufacturing techniques, which resulted in reduced coil resistance and a 24% increase in the motor constant [15,16]. Dehez et al. optimized the geometry of flexible printed circuit board (FPCB) coils, thereby maximizing back electromotive force (back-EMF) and minimizing resistance [17–21].
- Halbach Magnet Array Rotor: When optimizing a slotless PMSM with a Halbach array for copper loss minimization, research indicates that a configuration utilizing a magnetic rotor and NdFeB magnets achieves the highest efficiency with sinusoidal input current. This is attributed to its superior utilization of magnetic loading, outperforming configurations with NdFeB magnet arrays on nonmagnetic rotors [22]. Furthermore, studies have confirmed that optimizing the Halbach magnet array enhances electromagnetic torque [23].

Slotless motor windings include straight, oblique, and rhombic forms, each with distinct design and manufacturing requirements [24]. The complex three-dimensional conductor distribution challenges traditional 2D electromagnetic field simulations, which cannot accurately capture electromagnetic behavior. Currently, the mainstream simulation method, three-dimensional finite element analysis (FEA), while accurate, is cumbersome in modeling process and resource-intensive, limiting its engineering use [25]. Therefore, investigating simulation methods that can significantly reduce simulation time and enhance design efficiency, while maintaining accuracy, is highly significant, especially those suitable for preliminary design stages or large-scale parameter optimization scenarios.

Addressing this efficiency–precision dilemma, this study proposes a layered collaborative 2D electromagnetic simulation methodology. By integrating equivalent winding modeling and parametric scanning, the approach achieves minute-level simulation ef-

ficiency (approximately 40 times faster than 3D FEA) while maintaining accuracy. The method is applied to a 5 mm diameter, 50,000 r/min slotless PM motor for VAD applications, with prototype validation confirming its effectiveness.

This paper details the two-dimensional analysis method (Section 2), its application via EasiMotor [26] (Section 3), and prototype fabrication and testing (Section 4), providing a comprehensive workflow for rapid and accurate slotless motor design.

2. The Principle of Stratified Co-Simulation for a Slotless Motor

2.1. Hexagonal Winding Structure

Coreless windings primarily include oblique, hexagonal, and rhombic types (Figure 1). These windings are axially asymmetric; this study selects the typical stacked hexagonal winding for analysis. This configuration consists of straight and oblique segments, and the proposed methodology is applicable to other winding types.

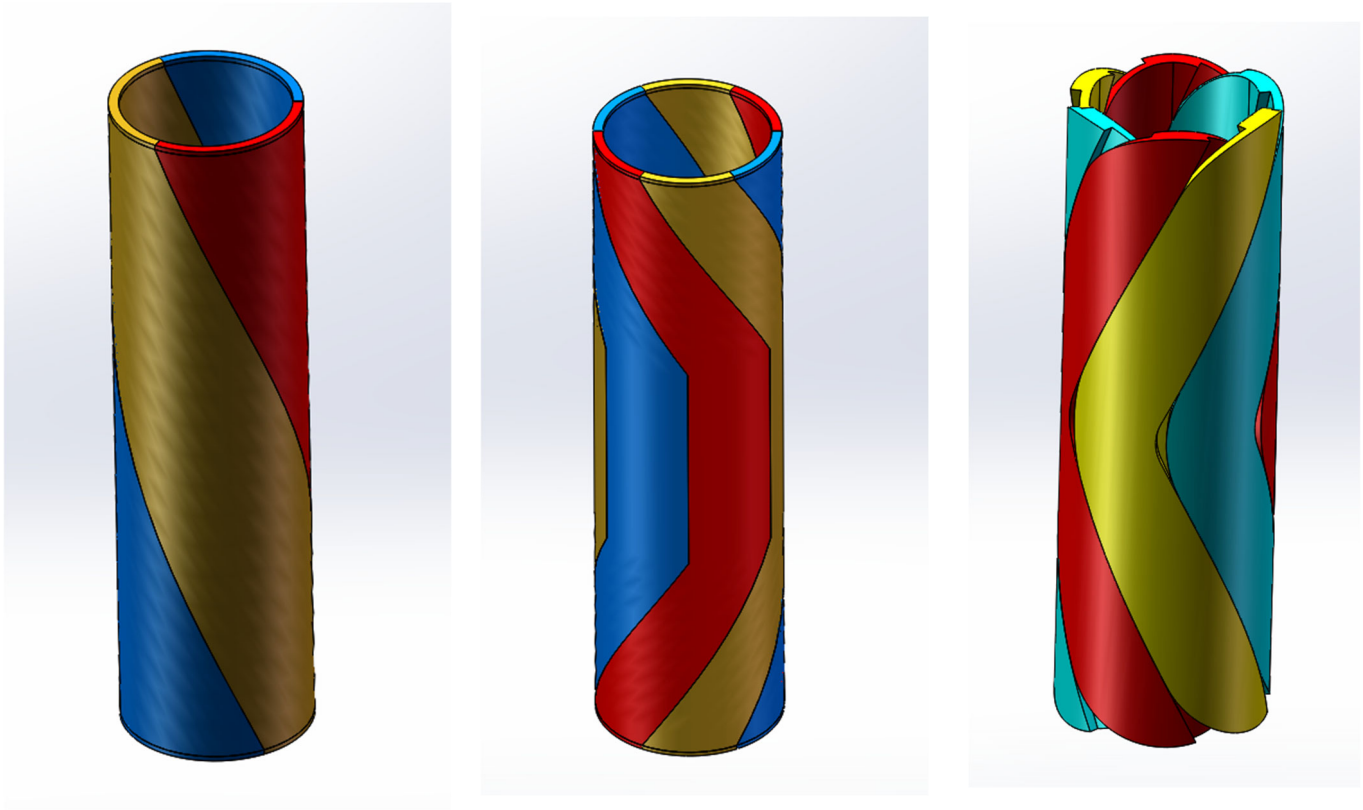

(**a**) (**b**) (**c**)

Figure 1. Three-dimensional structures of coreless windings (Each color represents a different phase): (**a**) oblique; (**b**) hexagonal; (**c**) rhombic.

The winding exhibits axial symmetry about the center plane. Due to this symmetry, the structure can be simplified into a half-period model for simulation purposes. In the case of the hexagonal winding, a single cross-section is chosen for the straight segments, and three equally spaced cross-sections are selected for the inclined segments. Each cross-section is modeled based on the actual geometry, resulting in four cross-sections used to accurately simulate a complete hexagonal coil (Figure 2).

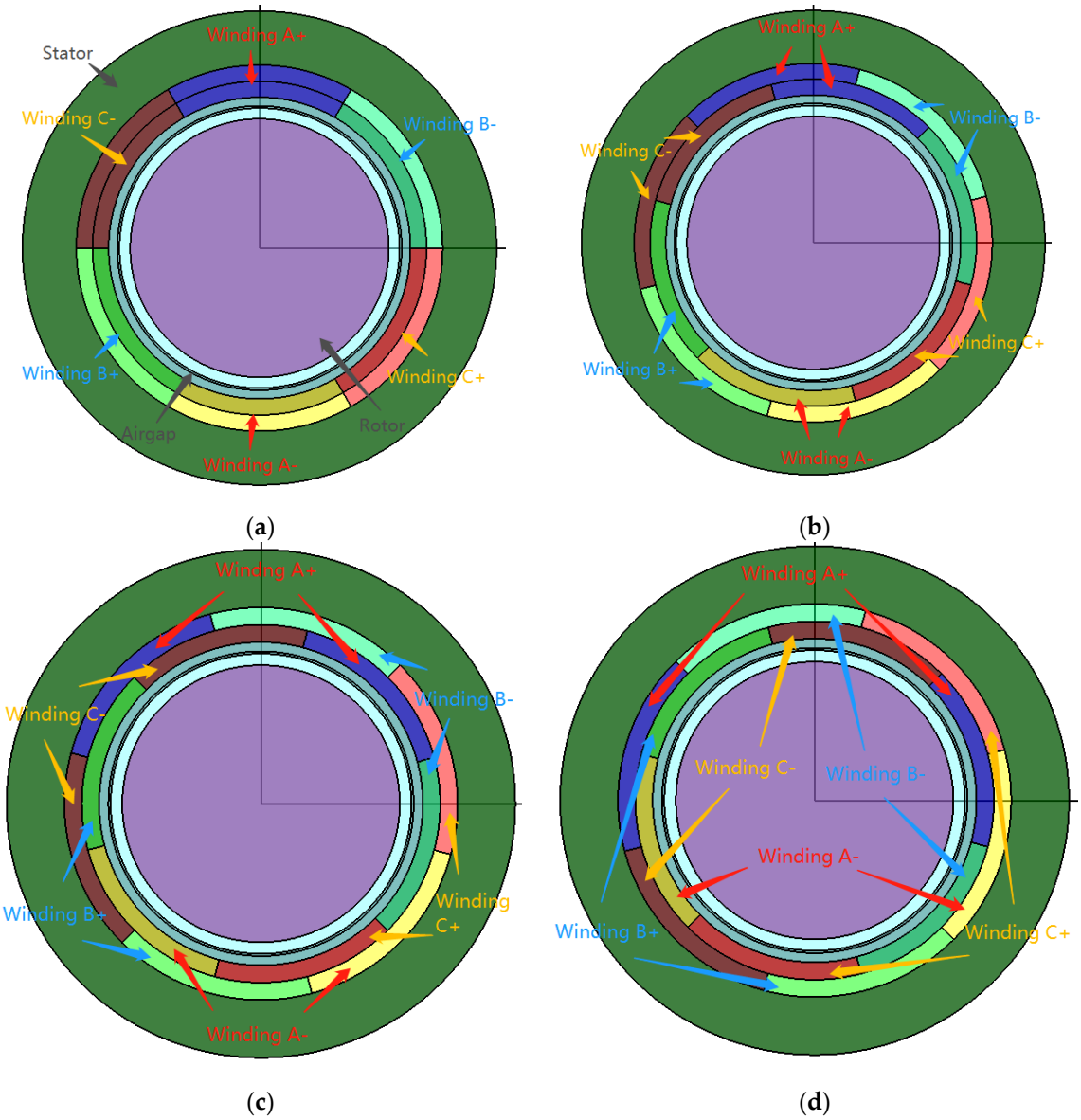

Figure 2. Four model cross-sections: (**a**) straight; (**b**) first inclined; (**c**) second inclined; (**d**) third inclined.

2.2. Technical Principle

The two-dimensional time-varying electromagnetic field in conventional straight-slot motors is governed by [27]:

$$\nabla \times (\nu \nabla \times A_Z) + \sigma \frac{\partial A_Z}{\partial t} = J_Z \tag{1}$$

where A_z is magnetic vector potential, and J_z is conduction current density.

The internal electrical circuit equation is calculated as follows:

$$U_S = R_S i_S + L_\sigma \frac{di_S}{dt} + \frac{d\Psi_S}{dt} \tag{2}$$

where U_s *is* winding terminal voltage; i_s is current in the winding; R_s is winding resistance; L_σ is winding leakage reactance; and Ψ_s is winding flux linkage.

The torque balance equation is calculated as follows:

$$J_m \frac{d\omega_m}{dt} + B\omega_m = T_{em} - T_L \tag{3}$$

where J_m is rotational inertia; B is friction coefficient; T_L is load torque; and T_{em} is electromagnetic torque, solved by Maxwell tensor method.

For slotless core motors, EasiMotor employs a segmented simulation approach [28] for analysis. Assuming the axial direction is divided into n segments, Equation (1) for the i-th segment becomes the following:

$$\nabla \times (\nu \nabla \times A_{\mathrm{Zi}}) + \sigma \frac{\partial A_{\mathrm{Zi}}}{\partial t} = J_Z \tag{4}$$

where A_{zi} is magnetic vector potential of the i-th segment, and J_z is conduction current density of the i-th segment.

Similarly, the voltage equations are reformulated as follows:

$$E_{\mathrm{i}} = -\frac{\mathrm{d}\Psi_{\mathrm{Si}}}{\mathrm{dt}} \tag{5}$$

$$U_S = R_S i_S + L_\sigma \frac{di_s}{dt} + \sum_{i=1}^{n} E_i \tag{6}$$

where E_i *is* induced voltage of the i-th segment, and Ψ_{si} is winding flux linkage of the i-th segment.

Equation (4) is discretized via finite element mesh splitting [27,29], coupled with Equations (3)–(6), enabling the solution of time-varying problems in slotless core motors.

The electromagnetic torque of the motor is equal to the following:

$$T_{\mathrm{em}} = \sum_{i=1}^{n} T_{em,i} \tag{7}$$

where $T_{em,i}$ is electromagnetic torque of the i-th segment.

2.3. Segments Parameter Calculation

The hexagonal winding consists of straight segments and two symmetrical triangular diagonal segments. Utilizing symmetry, only a half-model is necessary for axial simulation. The motor model is axially divided into n segments, with one cross-section extracted from each segment. The inclined segment is subdivided into $n - 1$ equal segments, with the midpoint of each segment selected as the simulation cross-sections. The coil unfolding schematic is shown in Figure 3.

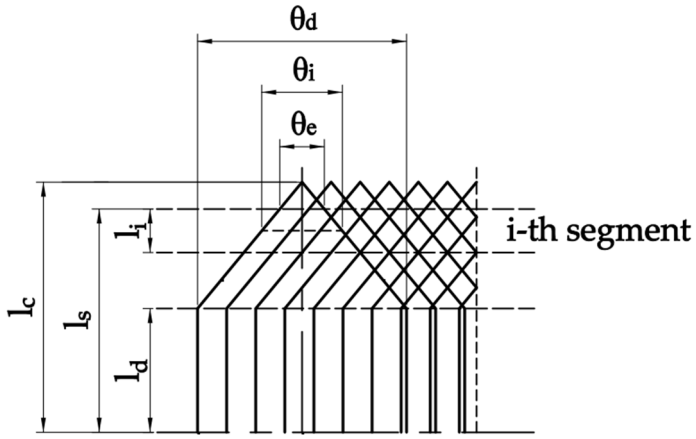

Figure 3. Schematic diagram of hexagonal coil dimensions.

The axial length of the i-th segment corresponding to the 2D finite element model is calculated as follows:

$$l_i = \frac{l_s - l_d}{n - 1} \tag{8}$$

The phase span angle of the i-th segment is calculated as follows:

$$\theta_i = \theta_e + (\theta_d - \theta_e) \times \frac{i - 0.5}{n - 1} \tag{9}$$

$$\theta_e = \left(1 - \frac{l_s - l_d}{l_c - l_d}\right)\theta_d \tag{10}$$

where l_c is the actual length of the wire cup; l_s is the calculated length of the wire cup; l_d is the length of the straight segment; θ_d is the span angle between the two coil sides; θ_i is the phase span angle of the i-th segment; and θ_e is the effective phase span angle at the end of the winding. When the winding length exceeds the length of the stator core, θ_e is the phase span angle at the coil aligns with the end of the core.

Since the axial cross-sectional models of oblique winding and rhombic winding are consistent with that of hexagonal winding, except that the axial length at the central cross-section is zero, the proposed method applies to all three winding configurations. Oblique winding and rhombic winding can be modeled as the lapped hexagonal winding with zero straight segment length (l_d = 0).

3. Motor Design

3.1. Requirements

The slotless motor is designed as a micro-motor for high-speed and high-flow pumps. Specifications are in Table 1.

Table 1. Slotless motor design specifications.

Design Specifications	Value Requirements
Rated Voltage	12 VDC
Rated Phase Current	≤0.7 Arms
Rated Power	2 W
Rated Speed	40,000 r/min
Maximum Speed	50,000 r/min
Rated Torque	0.8 mN·m
Motor Outer Diameter	5 mm
Motor Length	<25 mm
Number of Pole Pairs	2

3.2. Model

The slotless motor is simulated and designed using 2D finite element electromagnetic field analysis. Core, magnets, and other components follow conventional PMSM modeling; the focus is on equivalent winding modeling.

The hexagonal winding is equivalently modeled based on Section 2's winding model principles. The winding calculation length matches the stator stack height (15 mm). The straight segment is 5 mm; each oblique edge is 5 mm, divided into three 3.33 mm segments. The slotless winding's straight segment has a 180° span angle, yielding respective oblique segment angles of 150°, 90°, and 30°.

After equivalence, the 2D finite element electromagnetic simulation model is established (Figure 4).

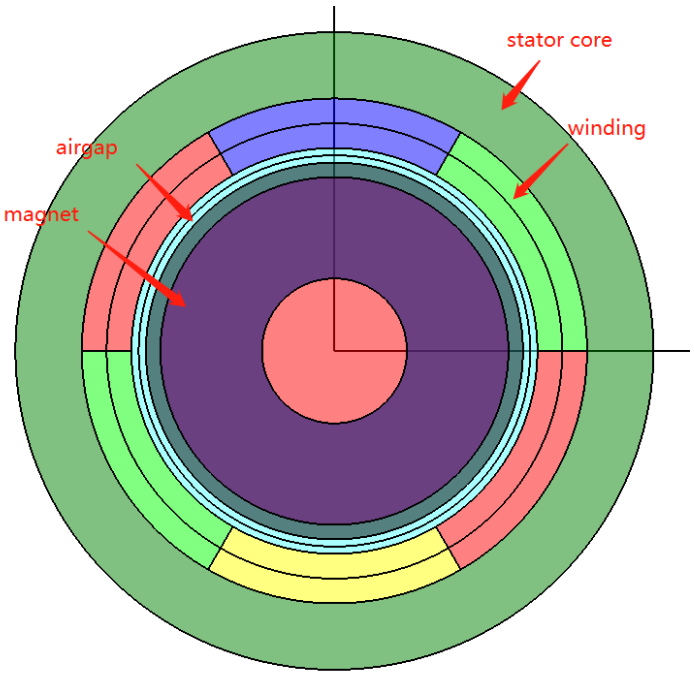

Figure 4. Two-dimensional finite element electromagnetic simulation model (Each color in the windings corresponds to a distinct phase).

Key dimensions and materials are listed in Table 2. The magnet is parallel magnetization with two poles. The residual magnetization B_r = 1.37 T, the coercivity H_{cb} = 1011 kA/m, and the intrinsic coercivity H_{cj} = 1592 kA/m.

Table 2. Slotless motor design parameters.

Parameters	**Value**
Stator Outer Diameter	4.5 mm
Stator/Magnet Length	15 mm
Rotor Shaft Diameter	1 mm
Air Gap	0.2 mm
Winding Length	15 mm
Number of Winding Layers	2
Components	**Material**
Slotless Winding	Copper
Stator Core	JFE_Steel_10JNEX900
Permanent Magnet	NdFeB N48SH

3.3. Optimization Design

After modeling, parametric scanning is applied to optimize the finite element model. The optimal solution is determined by maximizing output torque at a phase current of 0.7 A while maintaining the rated voltage at 12 VDC and a speed of 50,000 r/min. For star connection, the phase voltage amplitude limit is 6.928 VDC.

The primary design challenge involves selecting the appropriate winding parameters. Other dimensions are derived from these parameters: the stator inner diameter corresponds

to the winding outer diameter, and the magnet outer diameter is equivalent to the winding inner diameter minus twice the air gap.

Parametric scanning of winding turns (Figure 5) indicates that more than 16 turns result in excessive voltage, while fewer than 13 turns do not meet torque targets. Therefore, configurations with 14 and 15 turns are further optimized.

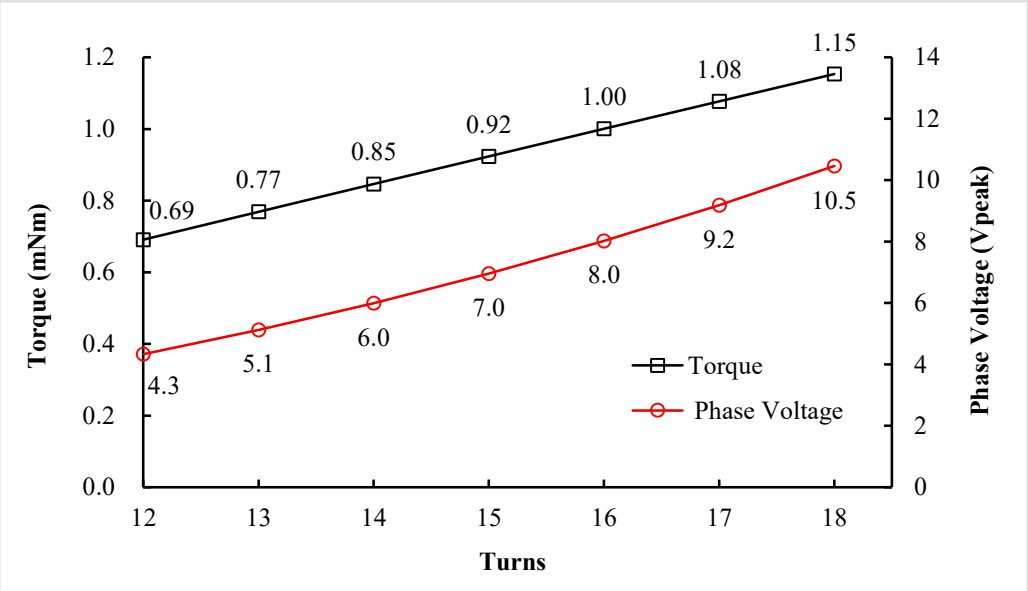

Figure 5. Effect of winding turns on output torque and phase voltage.

Further optimization of the winding diameter for 14- and 15-turn configurations (Figure 6) indicates peak torque at 2.75 mm (14-turn) and 2.8 mm (15-turn) pitch diameters, achieving minimized rated current required for the target, 0.8 mN·m torque.

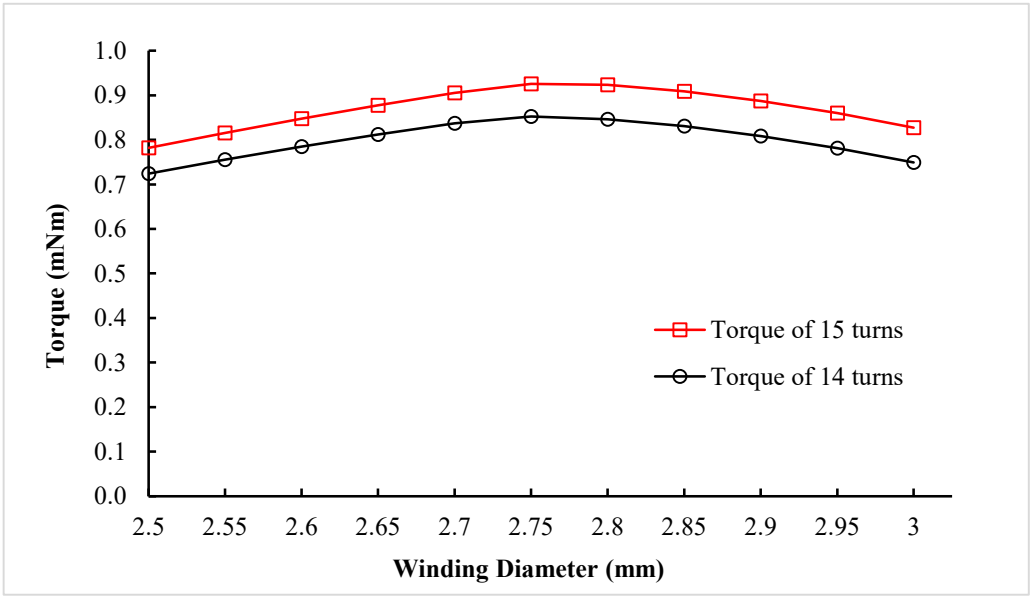

Figure 6. Effect of winding diameter on output torque.

Based on parametric scanning, the 15-turn configuration with 2.75 mm pitch circle diameter is identified as the optimal design for further development.

3.4. Two-Dimensional Optimal Solution Validation Simulation

A detailed 2D finite element electromagnetic field simulation was performed on the optimal solution derived from the preceding parameterized analysis. As illustrated in the waveform diagram Figure 7, the back-EMF waveform of the optimized design exhibited superior sinusoidal characteristics. At 50,000 r/min (corresponding to 833.3 Hz), the phase-back-EMF amplitude reaches 3.33 V.

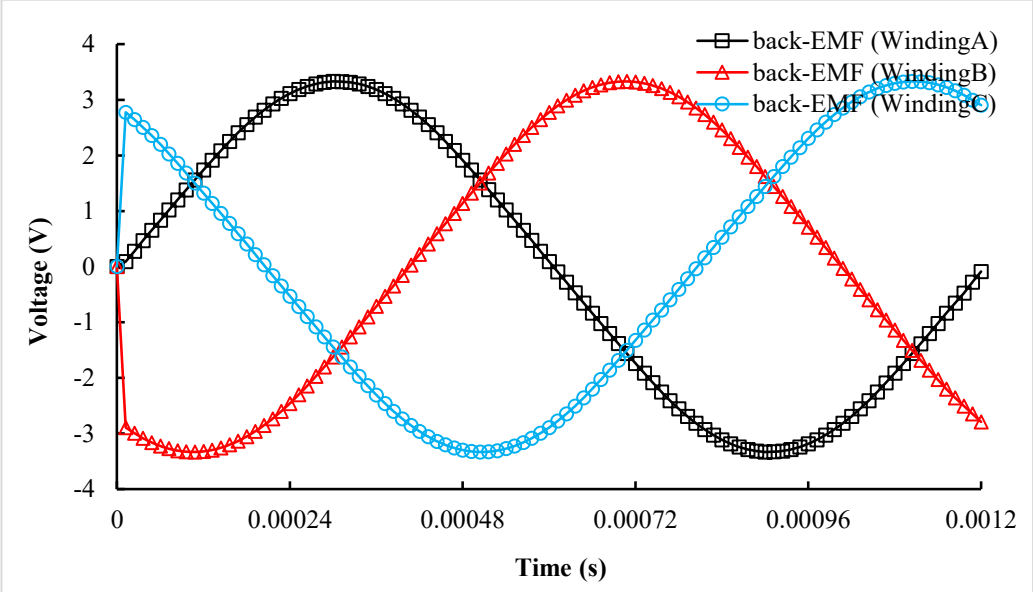

Figure 7. Back-EMF waveform of the optimal solution.

Given the surface-mounted rotor configuration, the direct-axis inductance (L_d) and quadrature-axis inductance (L_q) of the motor are essentially equal. Therefore, a current-source excitation mode with id = 0 was adopted under load conditions, assuming an ideal sinusoidal load current waveform.

Figures 8 and 9, respectively, present the current and torque curves under rated load conditions at 50,000 r/min. Parametric calculations for load conditions revealed that a phase current of 0.61 A could generate the target rated torque of 0.8 mN·m, achieving a 13% reduction compared to the design specifications, while limiting torque ripple to 0.5% (peak-to-average ratio).

The finite element analysis under load-conditions reveals that the stator flux density peaks at 1.8 T. Due to the strong permanent magnet flux of the motor, the no-load stator magnetic flux density is relatively high, and the magnetic field generated by the winding armature reaction has minimal impact on the permanent magnet magnetic field. Consequently, there is little difference between the no-load and loaded static magnetic fields at the same axial position (Figure 10).

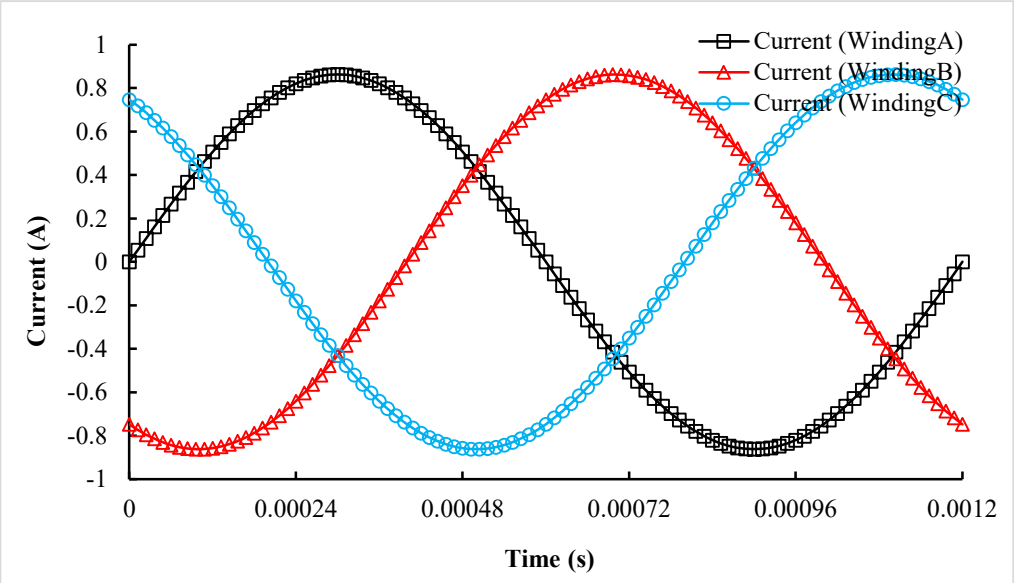

Figure 8. Rated load current waveform of the optimal solution.

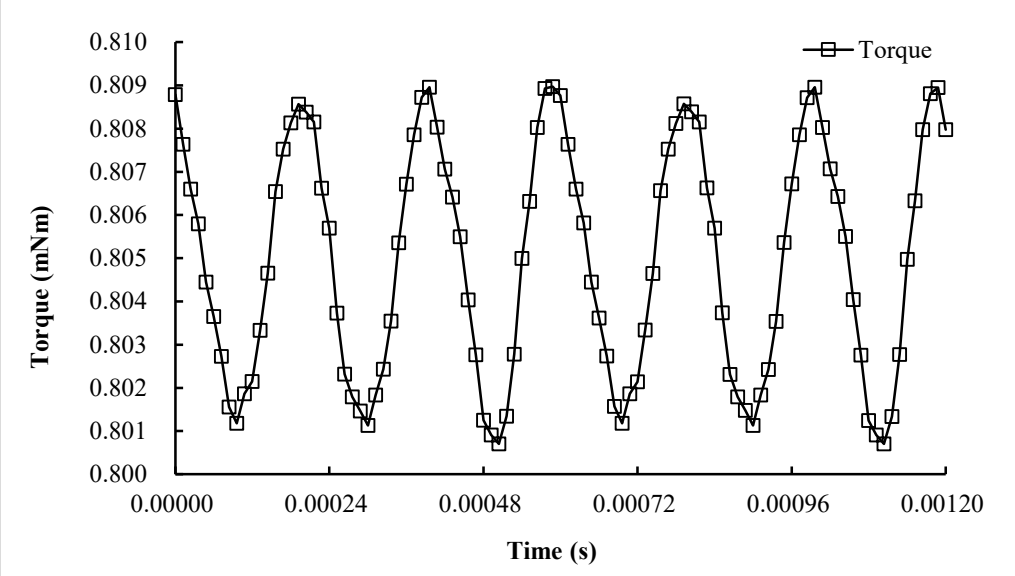

Figure 9. Rated load output torque waveform of the optimal solution.

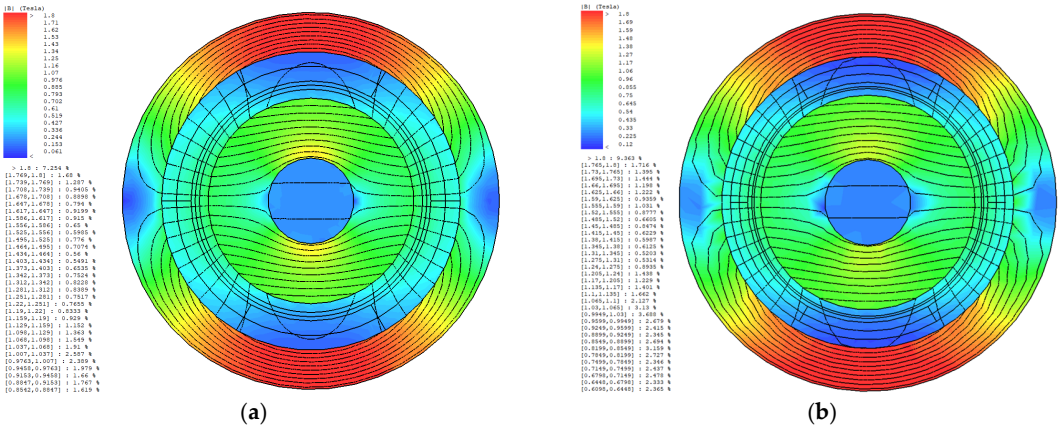

(**a**) (**b**)

Figure 10. Static magnetic field diagram of the optimal solution: (**a**) no load condition; (**b**) rated load condition.

The three-phase current density at different axial cross-section positions for the same time are shown in Figure 11.

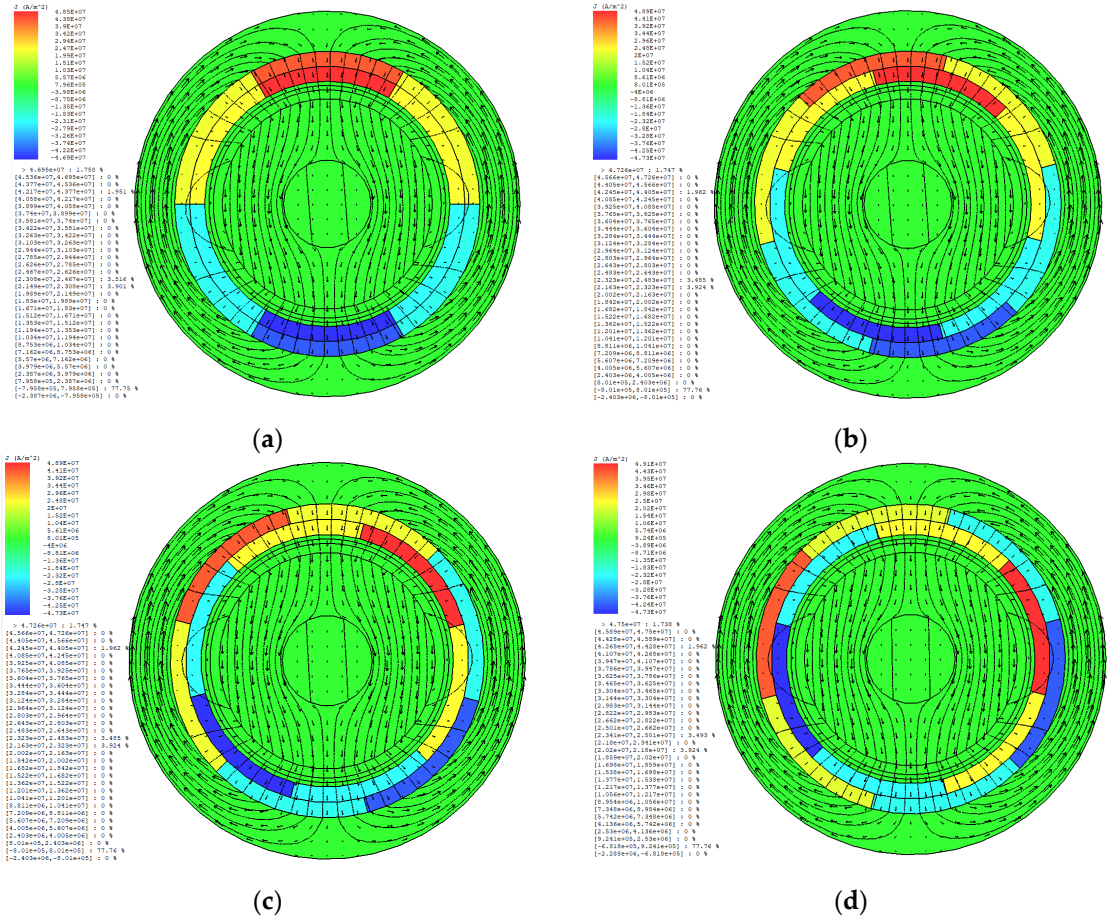

Figure 11. Rated load condition current density diagram in different axial cross-sections at the same time: (**a**) straight segment; (**b**) the first inclined segment of 150° winding span angle; (**c**) the second inclined segment of 90° winding span angle; (**d**) the third inclined segment of 30° winding span angle.

The current density diagrams at four different times for straight section are shown in Figure 12.

3.5. Three-Dimensional Optimal Solution Verification

To verify the accuracy of the 2D simulation model, a 3D finite element electromagnetic field model of the optimal solution was established for calculation, as shown in Figure 13. The winding model consists of a 5 mm long straight segment in the center and two 5 mm long inclined segments on either side.

The results obtained from the 3D model simulation were compared with those from the 2D model, as shown in the Figure 14 and Table 3. The amplitude of the phase back-EMF at 50,000 r/min is approximately 2% lower in the 3D model; the average output torque under a phase current of 0.61 A is also about 2% lower in the 3D model. The simulation errors between the two methods are within a small range, basically meeting design requirements.

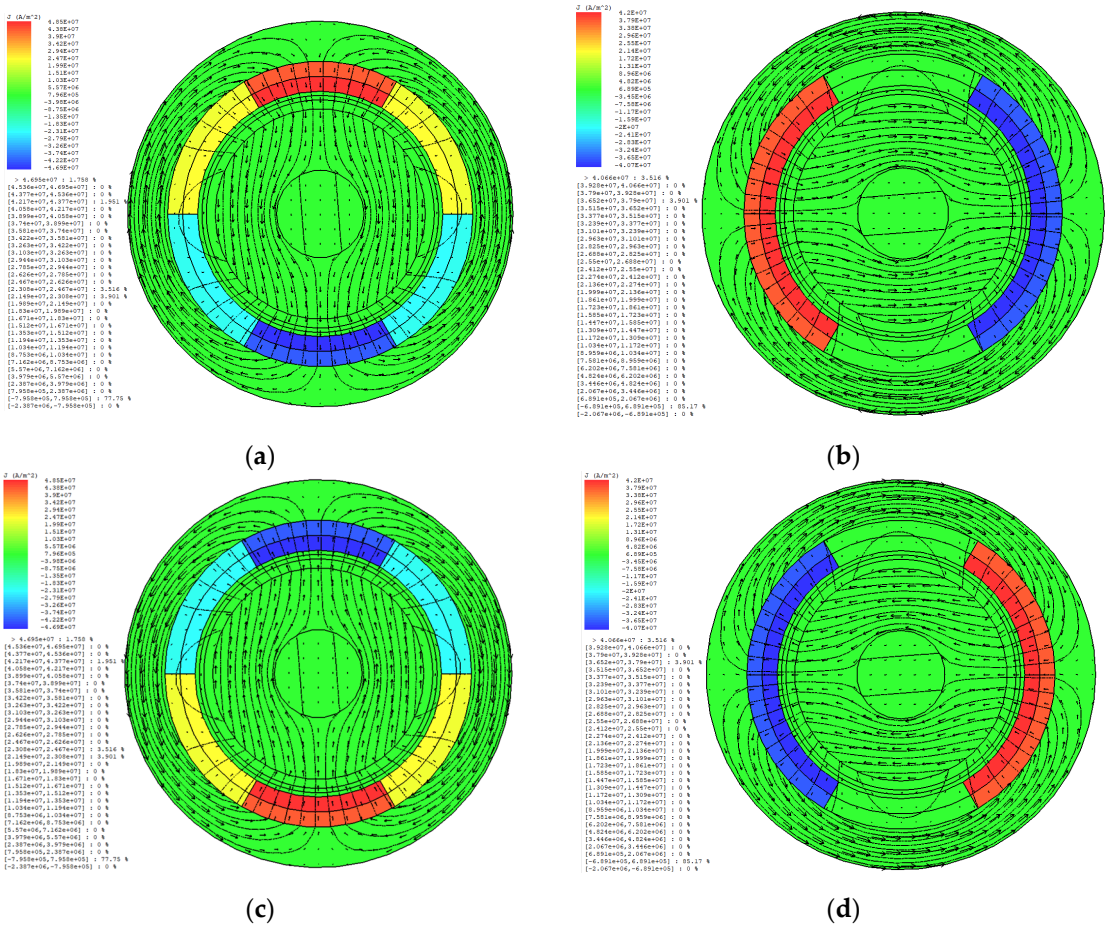

Figure 12. Rated load condition current density diagram in straight segment at the different time: (**a**) 0.0003 s, 1/4 electrical cycle; (**b**) 0.0006 s, half electrical cycle; (**c**) 0.0009 s, 3/4 electrical cycle; (**d**) 0.0012 s, one electrical cycle.

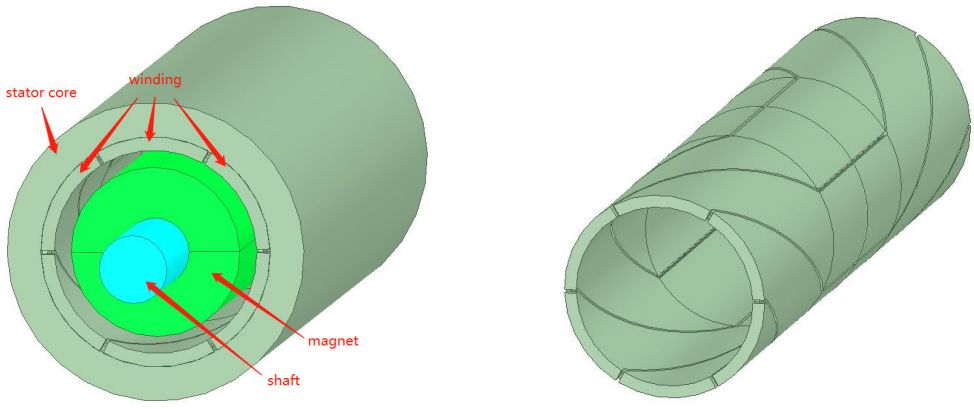

Figure 13. Three-dimensional finite element electromagnetic simulation model: (**a**) total model; (**b**) model of winding part.

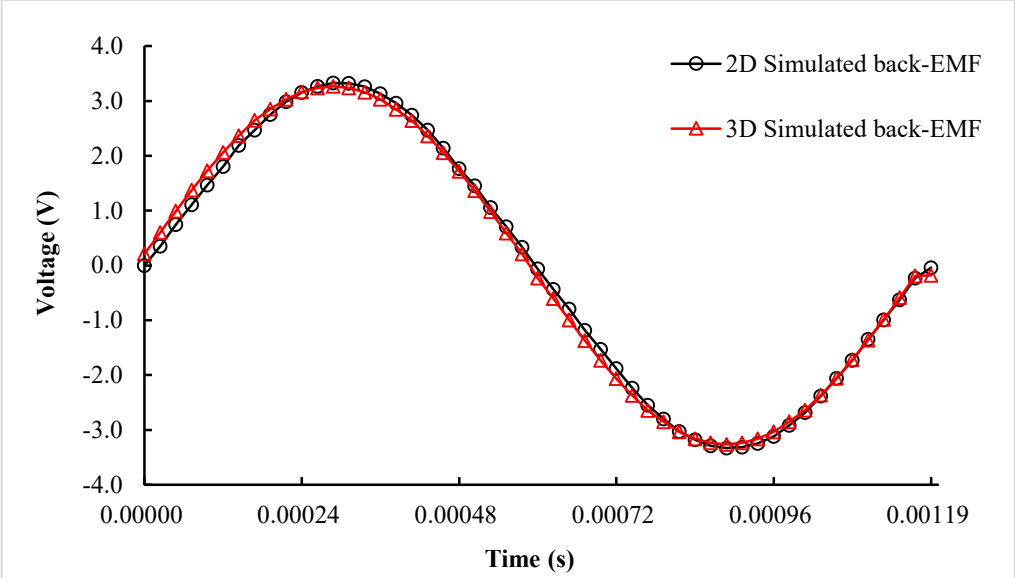

(**a**)

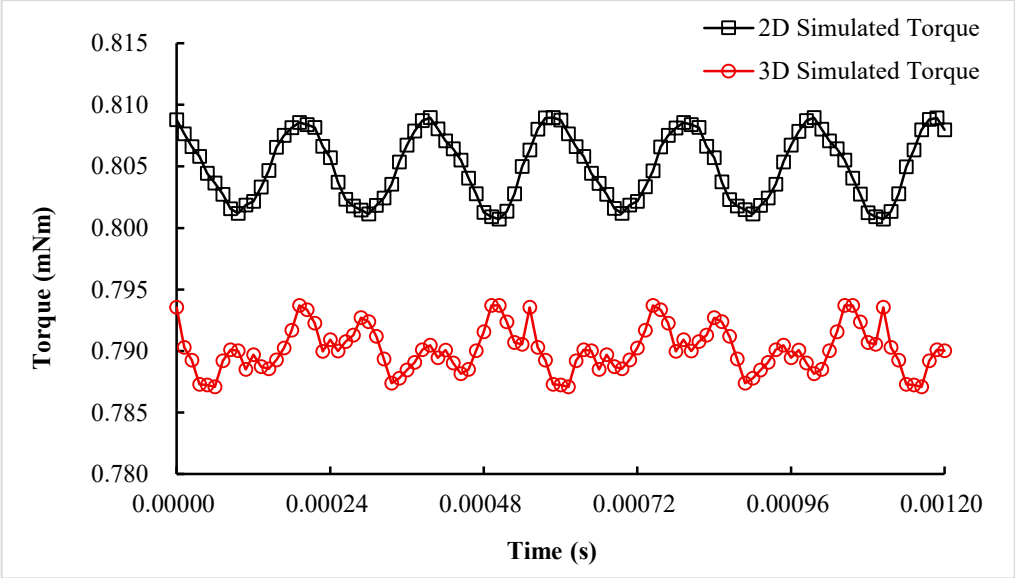

(**b**)

Figure 14. Comparison of simulation results between 2D and 3D models for the optimal solution: (**a**) phase back-EMF waveform; (**b**) rated load output torque waveform.

Table 3. Parameter table of the optimal solution.

Parameters	2D Model	3D Model
Phase Back-EMF Coefficient	0.667 V/kr/min	0.0653 V/kr/min
Torque Coefficient	1.32 mN·m/A	1.295 mN·m/A

4. Prototype Manufacturing and Testing

The prototype was fabricated based on the optimized design, Figure 15 illustrates some motor components, and Figure 16. outlines the assembly process flowchart of the prototype motor, Figure 17. demonstrates the practical implementation of assembly steps, Figure 18. presents the final assembled motor prototype.

The micromotor, featuring a slender shaft, is specifically designed for pump applications and has an impeller mounted on the output shaft. However, the torque is insufficient, and the shaft is too thin, rendering it untestable on the dynamometer. To precisely test the

back-EMF, a test tooling (Figure 19) was customized. In this setup, water pressure drives the rotor's rotation, while back-EMF signals are acquired through the oscilloscope and voltage probe.

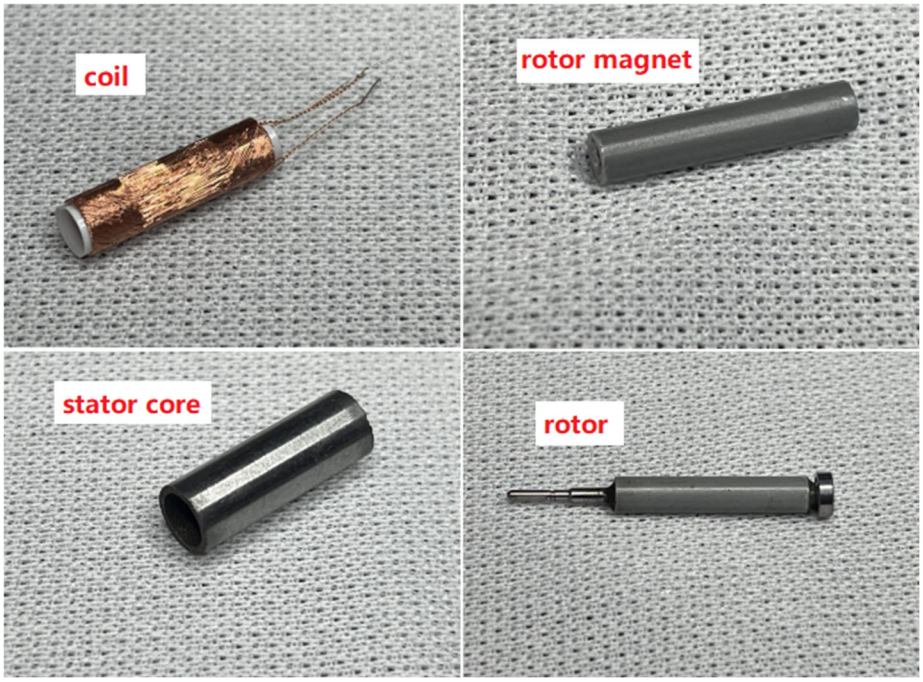

Figure 15. Prototype parts (coil, rotor magnet, stator core, rotor).

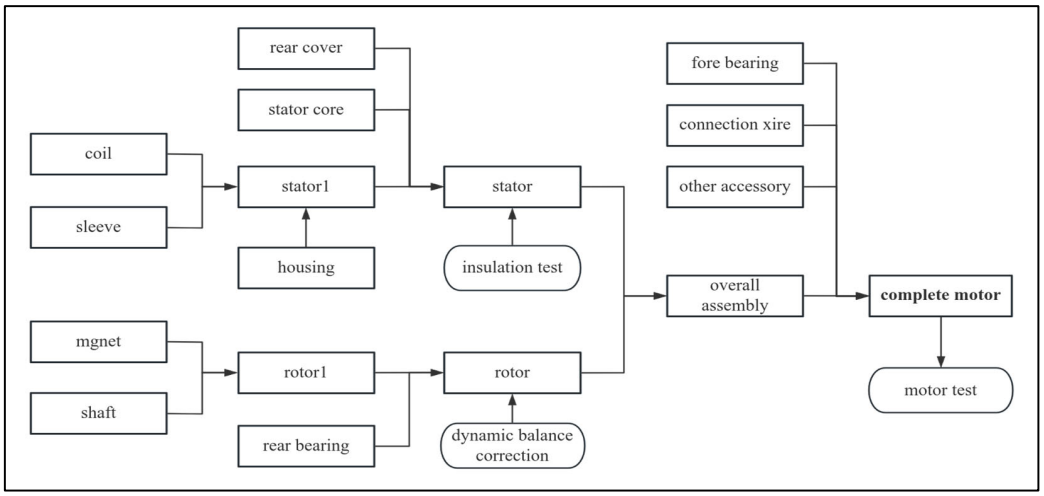

Figure 16. Simple diagram of the motor assembly process flowchart.



Figure 17. The practical implementation of the motor assembly steps. (1) coil and sleeve; (2) housing assembly; (3) stator core assembly; (4) rear cover assembly; (5) rotor assembly; (6) overall assembly; (7) completion of the motor.



Figure 18. Complete motor.



(**a**) (**b**)

Figure 19. Back-EMF test tooling: (**a**) installation compartment of the motor under test; (**b**) test system and water pump.

As shown in Figure 20, the 2D-simulated back-EMF deviates from the measured value by less than 2%. The minor variance can be attributed to the chamfers and dimensional deviations of the rotor magnets. The 3D simulated back-EMF has a deviation of less than 3% from the measured value. The 3D simulation curve shows certain harmonics, which can be

attributed to the insufficiently refined mesh. However, a finer mesh requires a significantly longer solution time. A 2D simulation case takes few minutes, while a 3D simulation takes over 3 h. The 2D simulation results are sufficiently accurate for engineering applications. Thus, the 2D simulation is considerably more efficient than the 3D simulation. With its high-efficiency solutions, the 2D simulation method is highly suitable for preliminary concept design and large-scale parametric design.

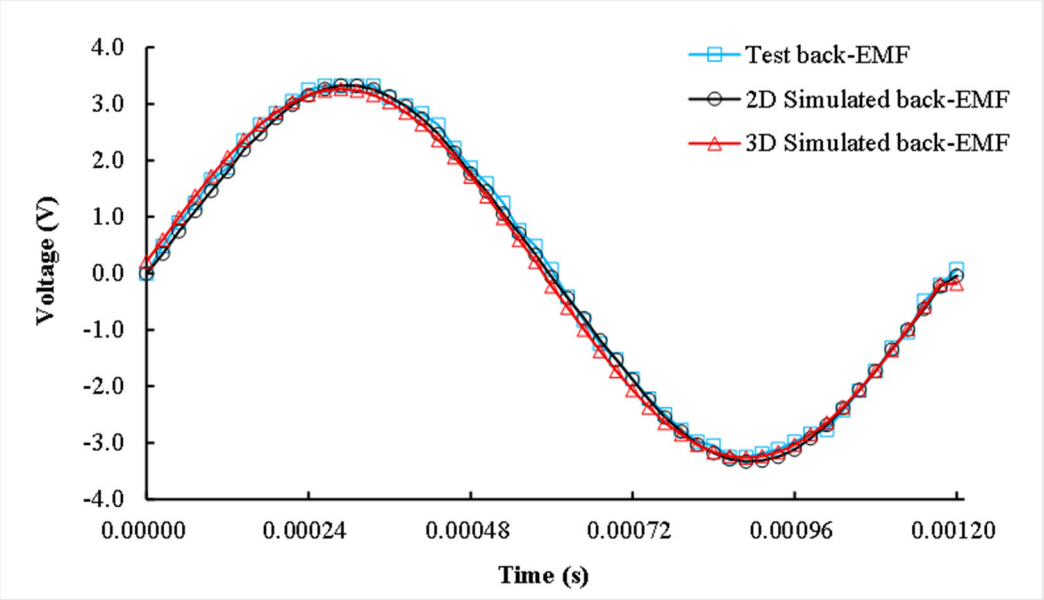

Figure 20. Comparison of simulated and tested back-EMF waveform at 50,000 r/min.

As shown in Figure 21, a motor under test equipped with an impeller pump and its associated components was placed in a water tank to conduct a loaded test.

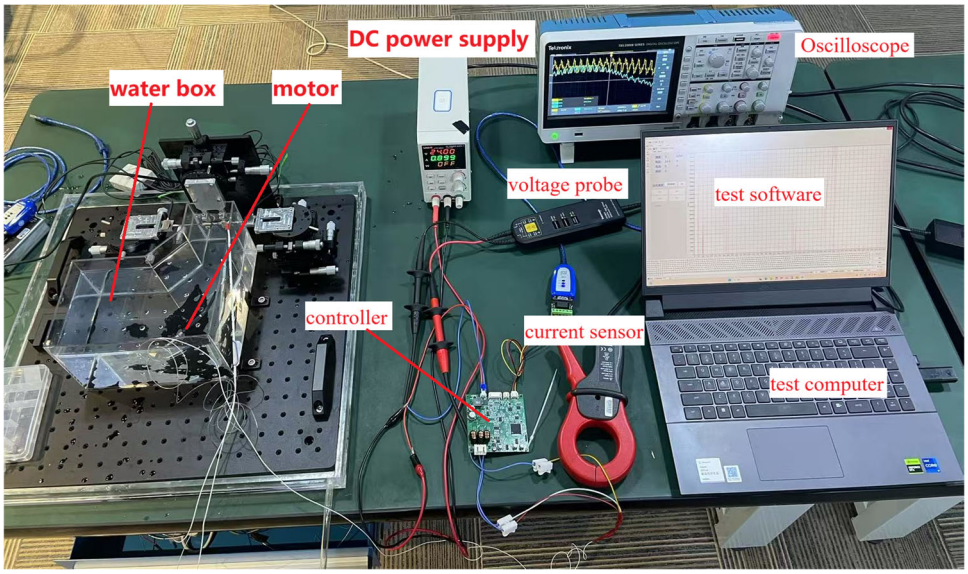

Figure 21. Motor with pump operation test system.

As illustrated in Figure 22, the current curve is shown when the motor operates with the pump impeller. The motor can reach speeds of up to 50,000 r/min, with a flow rate of 5 L/min. Due to its small inductance, switching-frequency harmonics are clearly observable in the current curve. The RMS line current measures 861.4 mA. Given the delta connection of the windings, the RMS phase current is 497.3 mA. The design current of 0.61

A was based on pump-head load estimation. The observed lower operational current of the vaned pump may stem from either overestimated load during design or the absence of outlet pressure, which reduces the actual load.

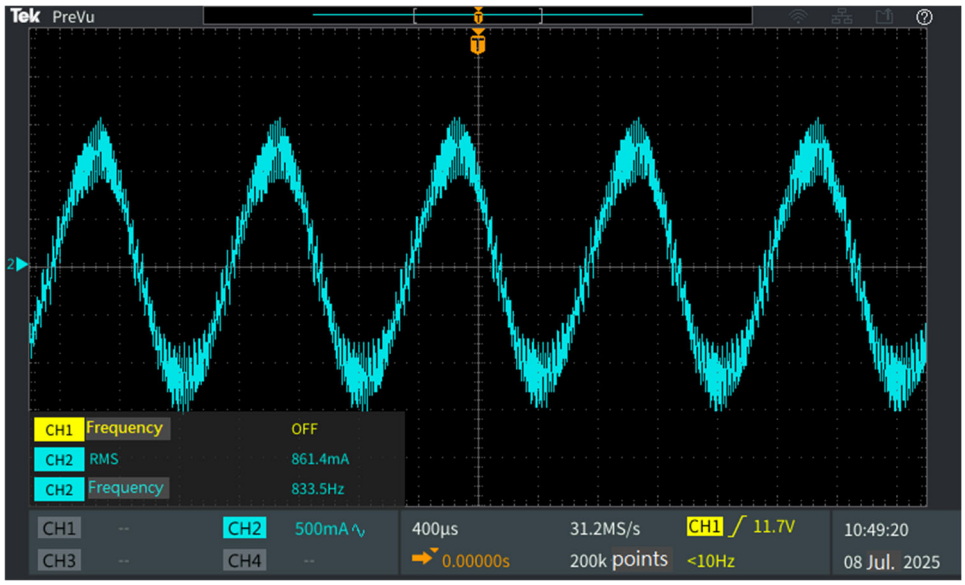

Figure 22. Current waveform of motor operating with pump impeller at 50,000 r/min.

5. Conclusions

A rapid 2D analysis method for slotless motor simulation is proposed using EasiMotor, covering the workflow from design to prototype validation. Key findings include the following:

- The novel 2D method overcomes traditional accuracy limitations, reducing simulation time to minutes while preserving electromagnetic fidelity, ideal for micromotor optimization.
- The 4.5 mm-diameter prototype exhibits back-EMF measurement errors within ±2% and stable performance at 50,000 r/min, validating the model's engineering utility.

Limitations and Future Work

- The proposed method effectively addresses coil length variations relative to stator core and rotor magnet dimensions but has not yet investigated scenarios where stator core and rotor magnet lengths differ. Future research will prioritize simulations for designs with mismatched stator core, rotor, and winding lengths to improve accuracy.
- Load decoupling tests were limited by the motor's low torque and the high dynamometer inertia, which prevented direct load measurements. Current tests rely on pump-head operation in water, which cannot quantify load torque–current relationships. Subsequent studies will focus on dynamometer-based load testing, loss separation, and thermal analysis for high-speed motors.
- A critical area for future exploration is bearingless magnetic suspension technology, which offers advantages such as eliminating material wear, reducing heat generation, and lowering sealing/corrosion resistance requirements. This innovation is particularly promising for applications like left ventricular assist pumps, where it minimizes red blood cell damage and thrombosis risks, thereby extending pump lifespan. Research on bearingless micromotors will be prioritized to leverage these benefits.
- The high-speed slotless micromotor presents control challenges due to its low stator inductance and high resistance, which result in rich current harmonics and elevated

losses. Enhancing control performance through advanced algorithms or topological optimizations remains essential [3,30,31].
- Future work should address nonlinear materials, thermal coupling, and intelligent manufacturing integration.

Author Contributions: Conceptualization, W.F. and Z.J.; methodology, W.F., Z.J. and S.Y.; software, T.L.; validation, Z.J. and J.X.; data curation, Z.J. and J.X.; writing—original draft preparation, Z.J. and L.Z.; writing—review and editing, S.Z.; supervision, Z.J. and W.F.; funding acquisition, W.F. All authors have read and agreed to the published version of the manuscript.

Funding: This research received no external funding.

Data Availability Statement: Data are contained within the article.

Conflicts of Interest: Authors Zhaohai Jin, Weizhong Fang, Jiawei Xu, Tianxiong Lu, Shitao Yang and Li Zhou were employed by the company Hangzhou Easitech Corporation. The remaining authors declare that the research was conducted in the absence of any commercial or financial relationships that could be construed as a potential conflict of interest.

References

1. Liu, C. Emerging Electric Machines and Drives—An Overview. *IEEE Trans. Energy Convers.* **2018**, *33*, 2270–2280. [CrossRef]
2. McKellar, S. A History of Mechanical Circulatory Support. In *Mechanical Support for Heart Failure*; Karimov, J., Fukamachi, K., Starling, R., Eds.; Springer: Cham, Switzerland, 2020. [CrossRef]
3. Wang, F.; Zhu, Y.; Wang, H.; Zhao, D. Design and Analysis of a Bearingless Permanent-Magnet Motor for Axial Blood Pump Applications. *IEEE Access* **2020**, *8*, 7622–7627. [CrossRef]
4. Sahnoune, A.; Hage-Hassan, M.; Krebs, G.; Marchand, C.; Guihaire, J.; Mercier, O. Design and analysis of a Circulatory Assistance Benchmark Actuator for an Artificial Lung. In Proceedings of the 2022 International Conference on Electrical Machines (ICEM), Valencia, Spain, 5–8 September 2022; pp. 827–833. [CrossRef]
5. Arslan, S.; Iskender, I. Design aspects of a 26500-r/min: 2-kw high-speed permanent magnet synchronous generator for turbomachinery systems. In Proceedings of the 2016 8th International Conference on Electronics, Computers and Artificial Intelligence (ECAI), Ploiesti, Romania, 30 June–2 July 2016; pp. 1–6. [CrossRef]
6. Liu, T.H.; Cheng, T.T. High-performance Micro-PMSM Control Systems including State-estimators. In Proceedings of the 2023 11th International Conference on Power Electronics and ECCE Asia (ICPE 2023—ECCE Asia), Jeju Island, Republic of Korea, 22–25 May 2023; pp. 675–680. [CrossRef]
7. Yan, G.J.; Lin, R.B.; Jian, M.H. Improvement on the core loss of high speed slotless PMBLDC motor and its measurement. In Proceedings of the 2012 15th International Conference on Electrical Machines and Systems (ICEMS), Sapporo, Japan, 21–24 October 2012; pp. 1–4.
8. Abdi, B.; Milimonfared, J.; Moghani, J.S. Simplified design of slotless halbach machine for micro-satellite Electro-Mechanical Batteries. In Proceedings of the 5th IET International Conference on Power Electronics, Machines and Drives (PEMD 2010), Brighton, UK, 19–21 April 2010; pp. 1–5. [CrossRef]
9. Lee, Y.S.; Jang, I.S.; Yang, I.J.; Kim, K.S.; Kim, W.H. Study on the Slotless PM Motor Design Process Considering High Speed. *IEEE Trans. Magn.* **2024**, *60*, 8203804. [CrossRef]
10. Bianchi, N.; Bolognani, S.; Luise, F. High speed drive using a slotless PM motor. *IEEE Trans. Power Electron.* **2006**, *21*, 1083–1090. [CrossRef]
11. Burnand, G.; Perriard, Y. Very-High-Speed Miniaturized Permanent Magnet Motors: Modeling and Experimental Validation. In Proceedings of the 2019 IEEE Energy Conversion Congress and Exposition (ECCE), Baltimore, MD, USA, 29 September–3 October 2019; pp. 5251–5257. [CrossRef]
12. Burnand, G.; Perriard, Y. Very-High-Speed Miniaturized Permanent Magnet Motors: Design and Optimization. In Proceedings of the 2019 IEEE Energy Conversion Congress and Exposition (ECCE), Baltimore, MD, USA, 29 September–3 October 2019; pp. 5258–5264. [CrossRef]
13. Burnand, G.; Araujo, D.M.; Koechli, C.; Perriard, Y. Validation by measurements of a windage losses model for very-high-speed machines. In Proceedings of the 2017 20th International Conference on Electrical Machines and Systems (ICEMS), Sydney, NSW, Australia, 11–14 August 2017; pp. 1–4. [CrossRef]

14. Burnand, G.; Araujo, D.M.; Perriard, Y. Very-high-speed permanent magnet motors: Mechanical rotor stresses analytical model. In Proceedings of the 2017 IEEE International Electric Machines and Drives Conference (IEMDC), Miami, FL, USA, 21–24 May 2017; pp. 1–7. [CrossRef]
15. Burnand, G.; Araujo, D.M.; Perriard, Y. Optimization of Shape and Topology for Slotless Windings in BLDC Machines. In Proceedings of the 2018 21st International Conference on Electrical Machines and Systems (ICEMS), Jeju, Republic of Korea, 7–10 October 2018; pp. 31–36. [CrossRef]
16. Burnand, G.; Thabuis, A.; Araujo, D.M.; Perriard, Y. Novel Optimized Shape and Topology for Slotless Windings in BLDC Machines. *IEEE Trans. Ind. Appl.* **2020**, *56*, 1275–1283. [CrossRef]
17. Dehez, B.; Baudart, F.; Perriard, Y. Comparison of FPCB windings of BLDC machines with paralelly and radially magnetized rotor poles. In Proceedings of the 2014 17th International Conference on Electrical Machines and Systems (ICEMS), Hangzhou, China, 22–25 October 2014; pp. 3331–3337. [CrossRef]
18. Baudart, F.; Dehez, B.; Denies, J.; Markovic, M.; Perriard, Y. Shape optimization of flexible PCB slotless windings in BLDC machines. In Proceedings of the 2013 International Conference on Electrical Machines and Systems (ICEMS), Busan, Republic of Korea, 26–29 October 2013; pp. 943–948. [CrossRef]
19. Dehez, B.; Baudart, F.; Markovic, M.; Perriard, Y. Theoretical and Experimental Investigation of Flex-PCB Air-Gap Windings in Slotless BLDC Machines. *IEEE Trans. Ind. Appl.* **2014**, *50*, 3153–3160. [CrossRef]
20. Dehez, B.; Baudart, F.; Perriard, Y. Analysis of a new topology of flexible PCB winding for slotless BLDC machines. In Proceedings of the 2017 IEEE International Electric Machines and Drives Conference (IEMDC), Miami, FL, USA, 21–24 May 2017; pp. 1–8. [CrossRef]
21. Verbeek, N.; Baudart, F.; Dehez, B. Preliminary comparison of slotless FPC winding and slotted wire winding PM machines. In Proceedings of the 2020 23rd International Conference on Electrical Machines and Systems (ICEMS), Hamamatsu, Japan, 24–27 November 2020; pp. 1892–1897. [CrossRef]
22. Jung, J.; Chattopadhyay, R.; Husain, I. Performance Evaluation of a Slotless Permanent Magnet Synchronous Machine with NdFeB/Ferrite Halbach Array under PWM Excitation. In Proceedings of the 2023 IEEE Energy Conversion Congress and Exposition (ECCE), Nashville, TN, USA, 29 October–2 November 2023; pp. 4393–4400. [CrossRef]
23. Ni, Y.; Qiu, Z.; Chen, J. Analytical Optimization of Slotless Surface-Mounted Halbach Magnet Machines. In Proceedings of the 2023 International Conference on Power Energy Systems and Applications (ICoPESA), Nanjing, China, 24–26 February 2023; pp. 846–851. [CrossRef]
24. Zhang, Q.; Chen, L.; Liu, A.; Yang, X. Characteristic Analysis of Slanting Winding and Concentric Winding of Coreless Motor. *Micromotors* **2020**, *48*, 22–24. [CrossRef]
25. François, G.; Baudart, F.; Henrotte, F.; Dehez, B. Numerical Investigation of Eddy Current Losses in Airgap PCB Windings of Slotless BLDC Motors. In Proceedings of the 2018 21st International Conference on Electrical Machines and Systems (ICEMS), Jeju, Republic of Korea, 7–10 October 2018; pp. 2702–2708. [CrossRef]
26. Liang, W.; Lu, T.; Zhang, X. Skew Effect Simulation Based on Multi-Slices Model. *Trans. China Electrotech. Soc.* **2011**, *26*, 135–140. [CrossRef]
27. Hu, M.Q.; Huang, X.L. *Motor Operation Performance Numerical Calculation Methods and Applications*; Southeast University Press: Nanjing, China, 2003.
28. Bastos, J.; Sadowski, N.; Dekker, M. *Electromagnetic Modeling by Finite Element Methords*; Marcel Oekker, Inc.: New York, NY, USA, 2003.
29. Jin, J. *The Finite Element Method in Electromagnetics*; John Wiley& Sonc, Inc.: New York, NY, USA, 2002.
30. Zad, H.S.; Khan, T.I.; Lazoglu, I. Design and Analysis of a Novel Bearingless Motor for a Miniature Axial Flow Blood Pump. *IEEE Trans. Ind. Electron.* **2018**, *65*, 4006–4016. [CrossRef]
31. Karabulut, Y.; Ayhan, U.; Aktaş, S.; Ayaz, M.; Meşe, E. Thermal Analysis of Small-Scale Axial Flux Permanent Magnet Synchronous Motors for LVAD Systems. *IEEE Trans. Ind. Appl.* **2025**, *61*, 3701–3710. [CrossRef]

Disclaimer/Publisher's Note: The statements, opinions and data contained in all publications are solely those of the individual author(s) and contributor(s) and not of MDPI and/or the editor(s). MDPI and/or the editor(s) disclaim responsibility for any injury to people or property resulting from any ideas, methods, instructions or products referred to in the content.